



Cite as

Nano-Micro Lett.
(2024) 16:164Received: 31 December 2023
Accepted: 17 February 2024
© The Author(s) 2024

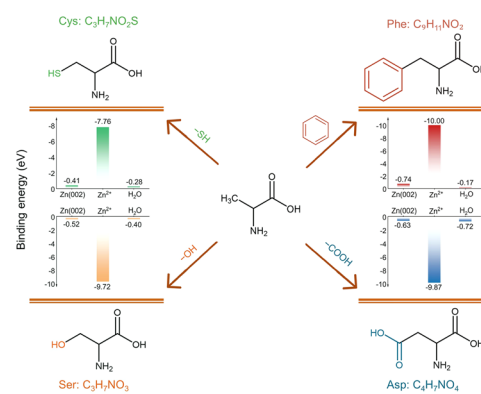
Amphipathic Phenylalanine-Induced Nucleophilic–Hydrophobic Interface Toward Highly Reversible Zn Anode

Anbin Zhou¹, Huirong Wang¹, Fengling Zhang¹, Xin Hu¹, Zhihang Song¹, Yi Chen¹, Yongxin Huang^{1,2} ✉, Yanhua Cui⁴, Yixiu Cui⁴, Li Li^{1,2,3}, Feng Wu^{1,2,3}, Renjie Chen^{1,2,3} ✉

HIGHLIGHTS

- The amphipathic phenylalanine-adsorbed layer contributes to form a nucleophilic–hydrophobic interface that homogenizes Zn²⁺ flux while repelling H₂O molecules from contacting Zn anode.
- The preferential reduction of phenylalanine (Phe) prior to H₂O facilitates *in situ* formation of an organic–inorganic hybrid solid electrolyte interphase, enhancing the interfacial stability.
- Benefiting from the triple protection of Phe, the Zn||Zn and Zn||LMO cells display significantly improved electrochemical performances, even at extreme diluted electrolytes.

ABSTRACT Aqueous Zn²⁺-ion batteries (AZIBs), recognized for their high security, reliability, and cost efficiency, have garnered considerable attention. However, the prevalent issues of dendrite growth and parasitic reactions at the Zn electrode interface significantly impede their practical application. In this study, we introduced a ubiquitous biomolecule of phenylalanine (Phe) into the electrolyte as a multifunctional additive to improve the reversibility of the Zn anode. Leveraging its exceptional nucleophilic characteristics, Phe molecules tend to coordinate with Zn²⁺ ions for optimizing the solvation environment. Simultaneously, the distinctive lipophilicity of aromatic amino acids empowers Phe with a higher adsorption energy, enabling the construction of a multifunctional protective interphase. The hydrophobic benzene ring ligands act as cleaners for repelling H₂O molecules, while the hydrophilic hydroxyl and carboxyl groups attract Zn²⁺ ions for homogenizing Zn²⁺ flux. Moreover, the preferential reduction of Phe molecules prior to H₂O facilitates the *in situ* formation of an organic–inorganic hybrid solid electrolyte interphase, enhancing the interfacial stability of the Zn anode. Consequently, Zn||Zn cells display improved reversibility, achieving an extended cycle life of 5250 h. Additionally, Zn||LMO full cells exhibit enhanced cyclability of retaining 77.3% capacity after 300 cycles, demonstrating substantial potential in advancing the commercialization of AZIBs.

KEYWORDS Zn anode; Phenylalanine; Adsorption energy; Solvation sheath

Anbin Zhou and Huirong Wang have contributed equally to this work.

✉ Yongxin Huang, huangyx@bit.edu.cn; Renjie Chen, chenrj@bit.edu.cn¹ Beijing Key Laboratory of Environmental Science and Engineering, School of Materials Science and Engineering, Beijing Institute of Technology, Beijing 100081, People's Republic of China² Advanced Technology Research Institute, Beijing Institute of Technology, Jinan 250300, People's Republic of China³ Collaborative Innovation Center of Electric Vehicles in Beijing, Beijing 100081, People's Republic of China⁴ Institute of Electronic Engineering, China Academy of Engineering Physics, Mianyang 621900, People's Republic of China

Published online: 28 March 2024

1 Introduction

Wearable and implantable electronics have rapidly evolved to meet the growing demands of modernized health care [1–3], including devices like smartwatches, cochlear implants, and cardiac pacemakers [4]. The sustained operation of implanted medical devices heavily relies on safe rechargeable batteries powering electronic circuitry for data acquisition, processing, and transmission [5]. Notably, aqueous Zn^{2+} -ion batteries (AZIBs) with inherently safe near-neutral electrolytes, superior biocompatibility, and higher energy density have gained significant attention [6–9]. However, the practical applications encounter some challenges such as dendrite growth and corrosion of Zn anodes, compromising long-term reliability [10–12]. Dendrite growth could puncture the separator and leads to battery short circuits, while Zn anode corrosion consumes active Zn and electrolyte, shortening its service life [13–15].

To enhance Zn anode reliability by inhibiting parasitic reactions or guiding uniform Zn deposition, various strategies, including electrode structure design [16–19], electrode interface modification [20–22], and electrolyte optimization [23–26], have been explored. Among these, the introduction of functional additives stands out as a feasible and effective approach with a substantial scale effect [27–29]. Previously, multiple mechanisms involving functional additives have demonstrated their role in achieving dendrite-free Zn anodes. For instance, the introduction of polar solvents like N-methyl-2-pyrrolidone (NMP) [30], N, N-dimethylformamide (DMF) [31], and acetone (DMK) [32] effectively optimizes the Zn^{2+} solvation sheath by replacing coordinated H_2O , thereby restraining H_2O -induced parasitic reactions and enhancing Zn reversibility. Additionally, the introduction of positively charged molecules with electrostatic preferential adsorption into the electrolyte induces an emerging progressive nucleation mechanism [27, 33, 34]. This mechanism stabilizes the Zn anode by homogenizing electric fields and regulating Zn deposition behavior. However, a single regulation strategy targeting solvation structure or molecule adsorption may not fundamentally shield the Zn anode from corrosion caused by free H_2O molecules [35].

Hence, it is crucial to explore multifunctional additives that simultaneously reduce H_2O molecule reactivity while constructing a robust hydrophobic protective interface. Amino acids, ubiquitous biomolecules, have gained attention

for their non-toxicity, biodegradability, and extensive use in the chemical industry as complexing agents and corrosion inhibitors [36, 37]. These molecules possess hydrophilic amino and carboxyl groups at either end and hydrophobic groups (e.g., methyl, isopropyl) in the middle, making them amphipathic compounds [38]. Their electron-rich nature enables excellent adsorption on metal electrode surfaces [37]. The hydrophilic units reduce interfacial free energy between the Zn electrode and electrolyte, facilitating Zn^{2+} transfer [39]. The hydrophobic groups form a local hydrophobic film of closer to the electrolyte, suppressing water-mediated parasitic side reactions [39]. Importantly, the precisely modifiable structure of hydrophobic groups allows for customizable additive design.

Based on the representative alanine, various derivatives with unique nucleophilic and hydrophobic characteristics can be created by grafting benzene ring, carboxyl, hydroxyl, and sulfhydryl groups onto the methyl, such as phenylalanine (Phe), aspartic acid (Asp), serine (Ser), and L-cysteine (Cys). Recent studies have shown that the aromatic molecules, such as benzoic acid, 3-hydroxytyramine hydrochloride, isophthalaldehyde, and 1,3-benzenedisulfonic acid disodium salt, embrace higher adsorption energy and stronger chemisorption effect on the Zn surface that promotes an even electric field distribution at electrode/electrolyte interface, inducing the uniform Zn deposition [40]. Therefore, the Phe featuring benzene ring ligands was introduced into AZIBs as electrolyte additive. The theoretical simulation and experimental evidence demonstrate that Phe (Figs. 1a and S1–S3) exhibits superior nucleophilic ability to coordinate with Zn^{2+} ions, efficiently regulating solvation to weaken H_2O molecule reactivity. Moreover, the unique lipophilicity of aromatic amino acids enables Phe to possess higher adsorption energy on the Zn (002) facet, contributing to form an nucleophilic–hydrophobic protective interphase [40]. The hydrophobic benzene ring ligands within Phe molecules form a hydrophobic film that repels H_2O molecules. Simultaneously, the adjacent hydrophilic carboxyl and hydroxyl groups attract Zn^{2+} ions to migrate to the Zn anode surface, guiding uniform Zn nucleation along the favorable (002) plane. Consequently, the addition of Phe at a concentration of 20 mmol L^{-1} demonstrates a beneficial impact by reducing the onset of hydrogen evolution (Fig. 1b), decreasing the corrosion current density, and concurrently increasing the corrosion potential (Figs. 1c and S4), which surpasses

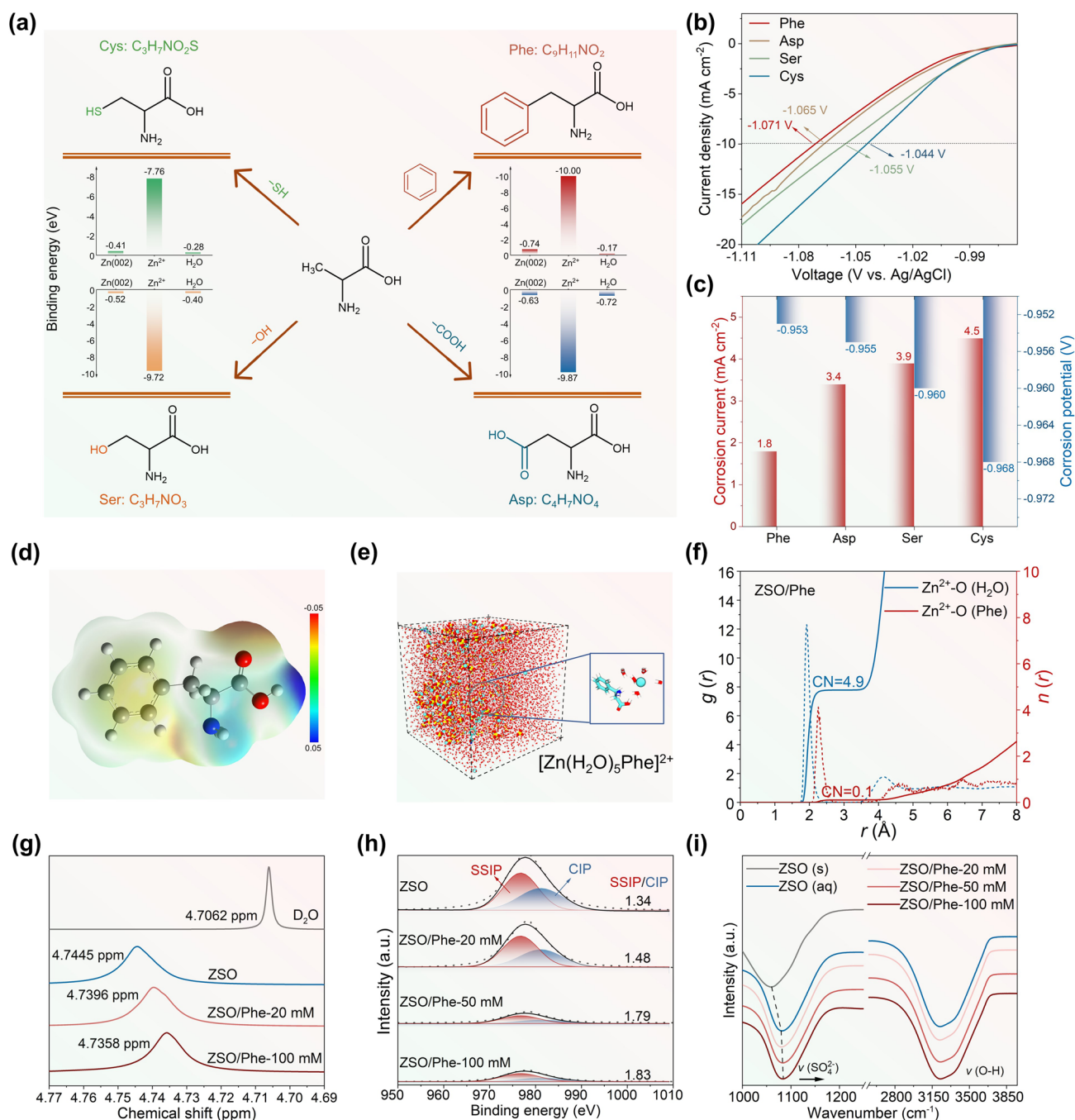


Fig. 1 Characterization of electrolyte system. **a** Schematic illustration for various derivatives of amino acids. **b** LSV curves and **c** corrosion current density and potential derived from Tafel plots in 20 mmol L⁻¹ Phe/Asp/Ser/Cys additives electrolytes. **d** Electrostatic potential mapping of Phe molecule. **e** Images of ZSO/Phe system obtained from molecular dynamics simulations. **f** Radial distribution functions for Zn²⁺-O (H₂O) and Zn²⁺-O (Phe) in ZSO/Phe electrolyte. **g** ²H NMR spectra of H₂O from pure D₂O, ZSO, and ZSO/Phe system. **h** Raman spectra and **i** FTIR spectra for ZSO and ZSO/Phe system with various concentrations

that of other derivatives in terms of corrosion inhibition. Finally, Zn||Zn symmetrical cells assembled using Phe-modified electrolytes exhibit enhanced Zn anode reversibility,

achieving an ultralong cycle life of 5250 h at 2 mA cm⁻², 2 mAh cm⁻², nearly 65 times higher than that in blank electrolytes, confirming its practical feasibility in AZIBs.

2 Experimental and Calculation

2.1 Preparation of Electrolytes and Electrodes

0.2 and 0.02 mol $\text{ZnSO}_4 \cdot 7\text{H}_2\text{O}$ (Aladdin, >99.99%) were dissolved in 100 mL deionized water, Phe (Adamas, >99%) solution (0.02 mol L^{-1}) to obtain 2 mol L^{-1} ZnSO_4 electrolyte, 0.2 mol L^{-1} ZnSO_4 -based dilute electrolyte, and 0.02 mol L^{-1} Phe containing electrolyte, respectively. $0.1 \text{ mol Li}_2\text{SO}_4$ (Macklin, >99.9%) was dissolved in above solution to obtain hybrid electrolyte. Commercial Zn foil ($100 \mu\text{m}$) polished with sandpaper was cut into 11-mm-diameter disks for preparing Zn anode. LiMn_2O_4 powders (Shenzhen kejing Co., Ltd), super-P carbon black (Nanjing XFNANO Materials Tech Co., Ltd), and polyvinylidene fluoride were mixed to form slurry at a weight ratio of 8:1:1. Then the slurry was coated onto Ti foil at a mass loading of 2.5 mg cm^{-2} and dried at $60 \text{ }^\circ\text{C}$ for 12 h to obtain LMO cathode.

2.2 Material Characterizations

Nuclear magnetic resonance (NMR, Bruker AVANCE III HD 600), Fourier transform infrared spectroscopy (FTIR, Bruker Alpha spectrometer), and Raman (Bruker RFS100/S) were conducted to characterize the electrolyte structure. The transmission electron microscopy (TEM, JEOL JEM 2800F), time-of-flight secondary ion mass spectrometer (TOF-SIMS, PHI nano TOF II), and X-ray photoelectron spectrometer (XPS, PHI-1600) with Ar^+ etching were employed to analyze the solid electrolyte interphase (SEI). The scanning electron microscopy (SEM, Hitachi SU-70), atomic force microscopy (AFM, Bruker Corp., Dimension Icon), and *in situ* optical microscope (Leica DVM6) were performed to investigate the Zn plating morphology. The *in situ* X-ray diffraction (XRD, Bruker AXS, WI, USA) and *in situ* differential electrochemical mass spectrometry (DEMS) were applied to characterize the phase structure change and monitor the H_2 production, respectively, during charging/discharging process.

2.3 Electrochemical Characterizations

CR2032-type coin cells (canrd, Canrd Technology Co. Ltd.) were assembled for $\text{Zn}||\text{Zn}$, $\text{Zn}||\text{Cu}$ and $\text{Zn}||\text{LMO}$

cells with glass fiber membrane soaked in $150 \mu\text{L}$ solution (DLAB Scientific Co., Ltd) to test the long-term galvanostatic cycling on a Neware battery test system (CT-4008 T-5V50mA-164, Shenzhen, China). Electrochemical impedance spectroscopy (EIS), cyclic voltammetry (CV) profiles, three-electrode-based measurements of Tafel plots, and linear sweep voltammetry (LSV) were performed on CorrTest CS350 electrochemical workstation (Wuhan Corrtest Instruments Corp., Ltd.).

2.4 Molecular Dynamics Simulations

The molecular dynamics simulations were conducted through GROMACS [41] with AMBER force field [42]. The MD parameters for SO_4^{2-} and amino acid molecule were generated through Sobtop [43], and the corresponding atom charges were based on RESP charges. The H_2O molecule was simulated with the simple point charge model. The initial size of box was $10 \times 10 \times 10 \text{ nm}^3$, and periodic boundary conditions were set in XYZ directions. The simulation cells contained 8200 H_2O , 300 ZnSO_4 , and 3 Phe. The electrostatic interactions were computed using PME methods. A cutoff length of 1.0 nm was used in the calculation of electrostatic interactions and non-electrostatic interactions in real space. The integration time step was 1 fs. The system was annealed from 0 to 298 K over a period of 0.5 ns, followed by running for another 2.0 ns to reach equilibrium. The temperature and pressure coupling was performed with V-rescale and Berendsen method, respectively. Finally, a 10 ns production simulation was carried out for post-processing analysis. The pressure coupling method in production simulation period was changed to Parrinello–Rahman.

2.5 Quantum Chemistry Calculations

Quantum chemistry calculations were conducted through Gaussian (G09) program. The structure optimization and energy calculations were performed at B3LYP-D3(BJ)/def2-SVP level. The calculations were carried out with the implicit universal solvation model based on solute electron density (SMD). The orbit was analyzed by Multiwfn package and VMD package [43].

2.6 Density Functional Theory Calculations

First-principles calculations were performed using the Castep module in Materials Studio 2019 with density functional theory [44]. The Perdew–Bruke–Ernzerh of exchange–correlation functional of the generalized gradient approximation (GGA) was adopted, and the cutoff energy with the value of 800 eV was used in all the calculations. The Γ -centered k-point grids were used for Brillouin zone integrations. The convergence criterion for the electronic structure iteration was set at 1×10^{-5} eV, while the geometry optimization was set to be 0.02 eV \AA^{-1} on force. The 7×7 supercell was used to model the Zn (002) surface, and a vacuum thickness of 15 \AA was applied. The atoms in the top two layers were free to simulate surface state, and the atoms in the other layers were fixed during calculation.

3 Results and Discussion

3.1 Characterization of Electrolyte System

The highly electronegative carboxylate groups within the Phe molecule exhibit robust nucleophilic characteristics due to the regional electron enrichment induced by benzene ring ligands (Fig. 1d), allowing them effectively coordinate with Zn^{2+} ions and optimizing the Zn^{2+} solvation environment [45]. Subsequently, molecular dynamics simulations were conducted to explore the structure of the Zn^{2+} solvation sheath on bare ZnSO_4 electrolyte (ZSO) and Phe-modified ZnSO_4 -based electrolyte (ZSO/Phe). As obtained from the radial distribution functions (RDFs) for Zn–O (H_2O) in ZSO electrolyte (Figs. S5 and S6), a characteristic peak emerged at around 2 \AA with an average coordination number (CN) reaching 5.2, suggesting that there are approximately six H_2O molecules coordinating with Zn^{2+} within the primary Zn^{2+} solvation shell. In contrast, after introducing Phe additive into the electrolyte, the Phe molecule intrudes the primary Zn^{2+} solvation structure and forms chelation with Zn^{2+} ions, as evidenced by the electrolyte box image of ZSO/Phe electrolyte system (Fig. 1e). Additionally, the peaks of Zn–O originated from both Phe and H_2O are positioned approximately 2 \AA away from Zn^{2+} , and the CN of Zn–O attributed to Phe and H_2O show around 0.1 and 4.9, respectively (Fig. 1f). These results further validate the ability of Phe molecules to integrate into the primary Zn^{2+} solvation

sheath and displace the partially solvated H_2O molecules. Typically, solvated H_2O molecules are deemed thermodynamically unstable at Zn deposition potential, representing a major contributing factor to the hydrogen evolution reaction (HER) [46]. Therefore, the orchestrated regulation of the Zn^{2+} solvation sheath is expected to curtail corrosion reactions induced by water molecules.

To delve deeper into the interaction mechanism of Phe additive in ZnSO_4 -based electrolyte, a series of analyses were conducted, including liquid-state NMR, FTIR, and Raman spectroscopy. As displayed in Fig. 1g, the ^2H peak of D_2O initially locates at 4.7062 ppm, while it shifts to 4.7445 ppm upon introducing ZnSO_4 into D_2O solvent, indicating a reduction in electronic density of hydrogen due to the charge transfer between Zn^{2+} and H_2O [47]. Subsequently, with the addition of 20 mmol L^{-1} Phe into the ZSO electrolyte, the peak position recovers to 4.7396 ppm. It gradually shifts to 4.7358 ppm with increased Phe concentration (up to 100 mmol L^{-1}), suggesting that the partially confined H_2O molecules within the Zn^{2+} solvation sheath are liberated. It is ascribed to the strong coordination effect between Phe molecule and Zn^{2+} ions that facilitated by higher binding energy [48]. Furthermore, in the Raman spectra analysis (Fig. 1h), the characteristic peak at 977 cm^{-1} is associated with the SO_4^{2-} ($\nu(\text{SO}_4^{2-})$), which can be deconvoluted into solvent-separated ion pair (SSIP) and contact ion pair (CIP) (Fig. S7) [48]. The SSIP/CIP ratio increases gradually with escalating Phe addition, reaching 1.83 at 100 mmol L^{-1} Phe concentration. This outcome confirms the involvement of Phe in the CIP by displacing SO_4^{2-} [48]. Additionally, the impact of Phe additive on Zn^{2+} coordination structure was corroborated by FTIR analysis (Fig. 1i). The vibration stretching of SO_4^{2-} ($\nu(\text{SO}_4^{2-})$) undergoes a noticeable blue shift from 1059.7 cm^{-1} (ZSO (s)) to 1080.2 cm^{-1} (ZSO (aq)) upon dissolving ZnSO_4 powder in H_2O solvent. This shift indicates weakened interaction between Zn^{2+} and SO_4^{2-} induced by primary Zn^{2+} solvation sheath formation [25]. Upon introducing 20 mmol L^{-1} Phe into the ZSO electrolyte, the $\nu(\text{SO}_4^{2-})$ shifts to 1081.9 cm^{-1} and further increases with higher Phe concentrations, reaching 1085.6 cm^{-1} at 100 mmol L^{-1} Phe additives. This indicates that the Phe additive weakens the electrostatic coupling between SO_4^{2-} and Zn^{2+} [25], confirming its influence on Zn^{2+} coordination structure. Furthermore, in the long-wavelength region of 2800–3700 cm^{-1} assigns three characteristic peaks to the O–H stretching vibration, corresponding to

strong H-bond (3147 cm^{-1}), weak H-bond (3307 cm^{-1}), and non-H-bond (3477 cm^{-1}) [30, 48], respectively (Fig. S8). As obtained from the H-bond proportion curves (Fig. S9), the intensity of strong H-bond gradually declines with Phe addition increasing, whereas the proportion of weak H-bond shows an upward trend. These observations suggest a suppression in the reaction activity of H_2O molecules.

3.2 Characterization of the SEI Chemistry

To analyze the electrolyte/electrode interface, the TOF-SIMS and XPS with Ar^+ sputtering depth profiling were employed. As shown in the XPS spectra of N 1s (Fig. 2a), the N-Zn (399.3 eV) and $-\text{NH}-\text{CO}-$ (401.4 eV) bands exclusively exist at the top surface (0 min, before sputtering) of Zn anode cycled in ZSO/Phe electrolyte, demonstrating the chemical adsorption of Phe molecules onto the Zn metal anode surface [35]. It is obviously observed that the ZSO/Phe electrolyte exhibits better wettability at 86.9° than ZSO electrolyte at 96.8° , which further confirms the strong adsorption ability of Phe molecules on Zn anode surface (Fig. S10). However, the contact angle between ZSO/Phe electrolyte and presoaked Zn anode of Phe-contained aqueous solution increases to 98.6° , exhibiting a hydrophobic tendency. As a contrast, the contact angle between ZSO/Phe electrolyte and presoaked Zn anode of deionized water remain nearly constant of 84.9° . This is ascribed to the adsorption of Phe molecules on Zn anode, where the hydrophobic benzene ring ligands toward the electrolyte, forming a molecular hydrophobic layer at the Zn/electrolyte interface, contributing to suppressing water-mediated parasitic side reactions. Additionally, the signals of C-H (283.8 eV) and C-N (285.5 eV) in the C 1s spectrum are detected at the top surface [23], diminishing significantly after 1 min of Ar^+ etching. Meanwhile, the characteristic peak of $\text{C}=\text{O}$ (530.8 eV) in the O 1s spectra displays relatively high intensity before sputtering but gradually fades away after 8 min of etching, indicating an organic layer predominantly covering the electrode top surface [48]. The higher highest occupied molecular orbital (HOMO, -6.5659 eV) and lower lowest unoccupied molecular orbital (LUMO, -0.7816) of Phe molecules compared to H_2O molecules (Fig. 2b) promote preferential electron acquisition by adsorbed Phe. These facilitate Phe reduction on the Zn anode surface ahead of H_2O to form a hydrophobic organic layer with minute

quantities of H_2 release [48]. In contrast, a series of new characteristic peaks in O 1s and S 2p spectra corresponding to ZnO (529.8 eV) [49], ZnS ($161.1/162.5\text{ eV}$) [50], and ZnSO_3 ($166.3/166.9\text{ eV}$) [50] emerge after 1 min of Ar^+ etching, and the intensities strengthen with increased etching time. This phenomenon demonstrates the *in situ* formation of ZnO, ZnS, and ZnSO_3 inorganic layers at the bottom of SEI. As shown in Fig. S11, the Phe molecule delivers higher binding energy of -4.47 eV with SO_4^{2-} compared to H_2O , which enables the SO_4^{2-} ions migrate to Zn anode surface favorably through Phe adsorption layer to be reduced by H_2 with *in situ* formation of ZnO–ZnS– ZnSO_3 inorganic layer [48]. Consequently, the Zn 2p spectrum exhibits significantly weaker intensity at the top surface (0 min, before sputtering) compared to the sample under Ar^+ etching (Fig. S12), attributable to both the chemically adsorbed film and the *in situ* organic SEI layer [51]. Furthermore, the existence of SO_4^{2-} ($168.5/169.9\text{ eV}$) on the Zn anode surface primarily originates from the precipitation of ZnSO_4 salt [48]. The TOF-SIMS was conducted to investigate the SEI chemistry induced by the Phe additive. Notably, the normalized intensity of organic CN^- and CH^- species decreases rapidly with increased sputtering depth, while that of ZnS, ZnO, and ZnSO_3 inorganic compounds increases significantly (Fig. S13). These observations indicate the uniform coverage of an organic layer composed of CN^- and CH^- species on the dense ZnS, ZnO, and ZnSO_3 inorganic layer, forming a gradient structure, as confirmed through three-dimensional (3D) visualization (Figs. 2c, S14, and S15). The organic layer enables the electrode/electrolyte interface with considerable deformability to accommodate the volume changes in repeated charging/discharging processes and excellent hydrophobic properties to protect the Zn anode from corrosion caused by active water molecules. Meanwhile, the ZnO/ZnS/ ZnSO_3 -rich bottom layer maintains high mechanical rigidity and rapid Zn^{2+} transport capability, enabling uniform Zn^{2+} ions flux for dendrite-free Zn deposition. On the contrary, the Zn anode cycled in ZSO electrolyte presents thimbleful C element and inorganic ZnO/ZnS/ ZnSO_3 species (Fig. S16). Obviously, almost no N element exists on the surface. To accurately determine the composition and structure of SEI formed in ZSO/Phe electrolyte, high-resolution TEM (HRTEM) was performed. The sample, prepared by depositing Zn^{2+} on copper micro-grids within Phe/ZSO electrolyte, revealed an ultrathin amorphous layer on the outer layer of the electrodeposited Zn particles in the high-angle annular

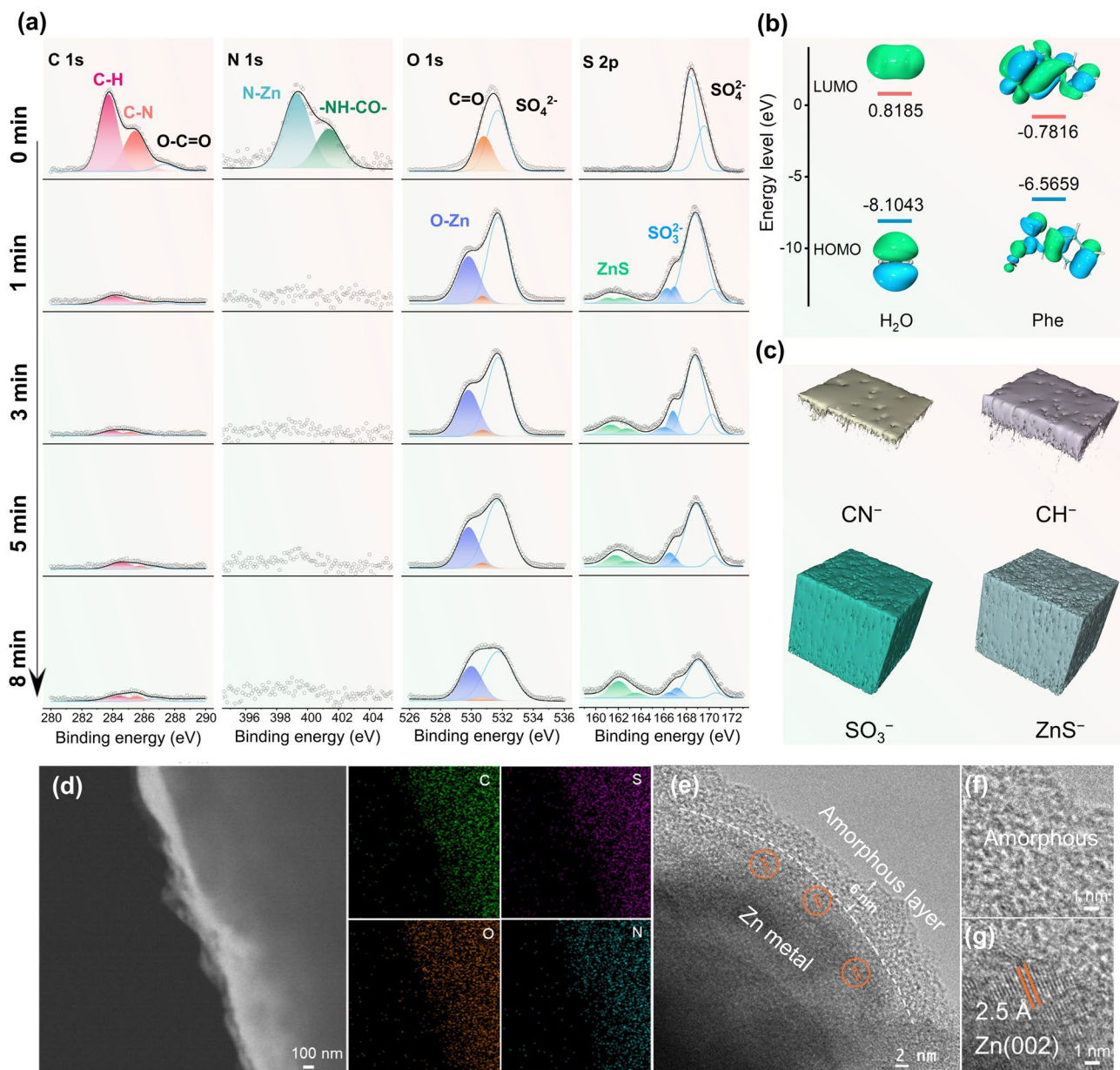


Fig. 2 Characterization of SEI chemistry. **a** XPS depth profile of C 1s, N 1s, O 1s and S 2p for Zn anode cycled in ZSO/Phe electrolyte for 5 cycles at a current density of 1 mA cm⁻². **b** HOMO–LUMO energy levels of Phe and water molecules. **c** 3D visualization of TOF–SIMS for CH⁻, CN⁻, SO₃⁻, and ZnS⁻ in ZSO/Phe electrolyte. **d** HAADF image. **e–g** HRTEM image of the electrode interface and corresponding elemental mapping

dark-field (HAADF) image (Fig. 2d). This amorphous layer is attributed to the *in situ* formed adsorption layer and SEI induced by the Phe additive. The energy-dispersive X-ray spectroscopy (EDS) mapping confirms the uniform distribution of the *in situ* constructed organic and inorganic hybrid SEI layer composed of C, N, O, and S elements on the surface of the Zn anode (Figs. 2d and S17). Furthermore,

HRTEM results reveal that the amorphous organic layer has a thickness of about 6 nm, and numerous lattice fringes of Zn (002) are observed inside the SEI layer (Fig. 2e–g). This suggests that the newly plated Zn is deposited through the protective interphase and preferentially grows with a favorable (002) plane during the initial deposition stage. As a result, a dual effect is achieved, simultaneously suppressing

the corrosion of water molecules and inhibiting the formation of Zn dendrites.

3.3 Characterization of the Interfacial Interaction

To comprehensively comprehend the protective mechanism of the Phe additive in stabilizing the Zn anode and controlling deposition behavior, *in situ* Raman spectroscopy was employed within Zn||Zn symmetrical cells cycled in different electrolytes. As indicated in Fig. 3a, the Zn anode cycled in ZSO electrolyte displays a distinct characteristic peak at 362 cm^{-1} , which is attributed to the aggregation of $\text{Zn}(\text{OH})_4^{2-}$ induced by HER [52], revealing the vigorous

corrosion reaction during Zn plating. The peak around 916 cm^{-1} , attributed to $\nu(\text{SO}_4^{2-})$ vibration [28], exhibits a slight decrease due to participation in interface side reactions. Conversely, the cell with ZSO/Phe electrolyte did not exhibit $\text{Zn}(\text{OH})_4^{2-}$ by-product enrichment. It is attributed to the collaborative action of the Phe adsorption film, *in situ* SEI formation, and regulation of Zn^{2+} coordination environment that collectively restrains the decomposition of H_2O molecules. Furthermore, the XRD patterns of Zn anodes cycled in ZSO electrolyte reveal characteristic peaks at 7.9° , 16.1° , and 24.3° corresponding to $\text{Zn}_4(\text{OH})_6(\text{SO}_4)_4 \cdot 5\text{H}_2\text{O}$ by-products, indicating rampant HER at electrode interface (Fig. 3b) [47]. In contrast, a pure Zn anode can be attained

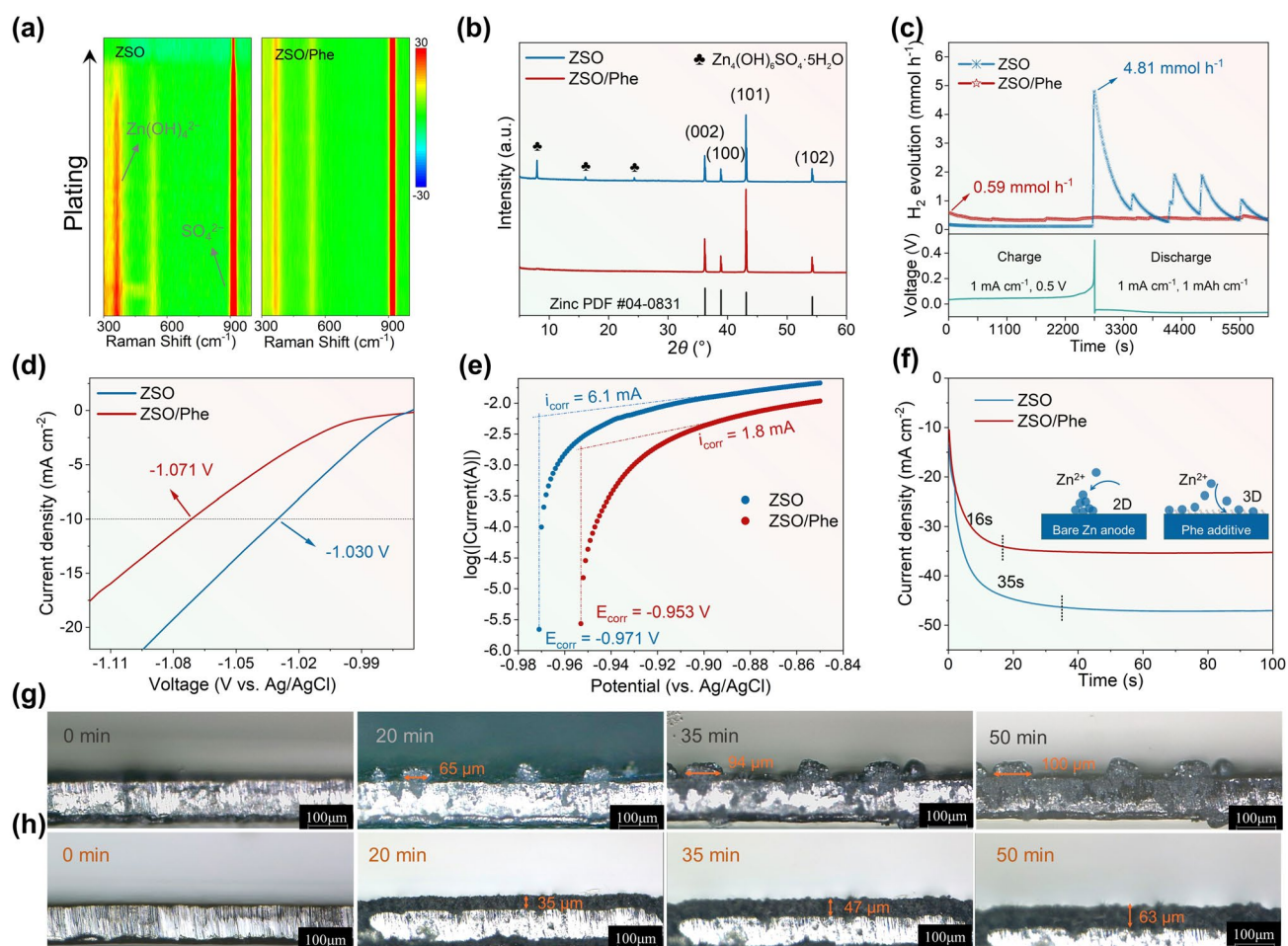


Fig. 3 Characterization of interfacial interaction. **a** *In situ* Raman spectrum for Zn anode tested in ZSO and ZSO/Phe electrolytes in Zn^{2+} plating process. **b** XRD patterns of cycled Zn anodes. **c** *In situ* DEMS measurement of H_2 evolution rate within Zn||Cu cells. **d** LSV curves and **e** Tafel plots of Zn electrodes measured in ZSO and ZSO/Phe electrolytes. **f** CA curves at an overpotential of -150 mV within Zn||Zn cells (inset: schematic diagrams of 2D and 3D diffusion process of Zn^{2+}). *In situ* optical microscopic images of Zn plating process in **g** ZSO and **h** ZSO/Phe electrolytes

in the ZSO/Phe electrolyte, aligning with the *in situ* Raman spectra results. To quantitatively analyze the HER reaction rate, *in situ* differential electrochemical mass spectrometry (DEMS) was carried out on Zn||Cu half cells with different electrolytes. As displayed in Fig. 3c, the H₂ evolution rate in the ZSO electrolyte sharply increases to 4.81 mmol h⁻¹ at 0.5 V, indicating severe corrosion reactions during Zn plating. By contrast, the cell employing ZSO/Phe electrolyte displays significantly suppressed HER, registering only 0.59 mmol h⁻¹ at the early charging step. On the one hand, the amino and carboxyl groups are liable to chelate with Zn²⁺ for weakening the reactivity of solvated H₂O molecules. The lower onset HER potential of ZSO/Phe electrolyte, deduced from linear scanning voltammetry (LSV), further supports the aforementioned results (Fig. 3d). On the other hand, the hydrophobic groups, including benzene ring, and the Phe-induced SEI together constitute a drainage layer that restrains the H₂O-mediated parasitic side reactions. For an accurate assessment of anti-corrosion capability, corrosion current density and corrosion potential were investigated through Tafel plots (Fig. 3e). Remarkably, the Zn anode in ZSO/Phe electrolyte exhibits a more positive corrosion potential (-0.953 vs. -0.971 V) and lower corrosion current density (1.8 vs. 6.1 mA cm⁻²) compared to that in ZSO electrolyte, confirming the superior performance of Phe additive in inhibiting side reactions. Besides, the Zn²⁺ diffusion behavior on the Zn anode surface was analyzed via the chronoamperometry (CA) curves. The current density for Zn||Zn cells tested in ZSO/Phe electrolyte rapidly stabilizes at -35.4 mA cm⁻² after a short 2D diffusion process at an overpotential of -150 mV on the Zn anode (Fig. 3f), demonstrating a sustained 3D diffusion process after nucleation. The hydrophilic units reduce the interfacial free energy between the Zn electrode and the electrolyte while attracting the Zn²⁺ ions migration to Zn anode surface, guiding the Zn²⁺ homogeneous deposition (inset in Fig. 3f). In contrast, the Zn||Zn cell in ZSO electrolyte displays continuous current density increase within 35 s, indicating a rampant 2D diffusion with lateral Zn²⁺ diffusion along the surface and deposition at the most favorable energy position. This may lead to potential safety hazard with dendrite growth and short circuit [49]. Subsequently, the actual Zn²⁺ deposition process was examined by *in situ* optical microscopy, revealing randomly distributed protrusions on the Zn anode surface during electrodeposition in ZSO electrolyte (Fig. 3g). The size of protrusions on the Zn anode surface increases

from 65 to 100 μm as deposition time increasing from 20 to 50 min. In addition, distinctly irregular interface is observed on the Zn anode surface after 50 min of plating in the ZSO electrolyte (Fig. S18), resulting in Zn dendrite formation finally. In sharp contrast, a uniform and dense dendrite-free Zn deposition layer with 63 μm thickness is observed on the Zn anode surface after 50 min of plating in the ZSO/Phe electrolyte (Fig. 3h), which further confirms the positive effect of adsorbed Phe molecules and the well-defined SEI layer in promoting uniform Zn²⁺ ions deposition.

3.4 Reversible Zn Plating/Stripping Stability Characterization

To certificate the protective effect of Phe additive on the stability and reversibility of Zn anode, extensive galvanostatic cycling experiments were conducted on Zn||Zn symmetrical cells and Zn||Cu half cells. As shown in Fig. 4a, the symmetrical cells with ZSO electrolyte experience rapid short-circuiting after only 80 h of cycling due to rampant dendrite growth (Fig. S19). In contrast, the cells utilizing ZSO/Phe electrolyte demonstrate an extended lifespan exceeding 5250 h with a high overpotential of approximately 138 mV at 2 mA cm⁻², 2 mAh cm⁻² (Fig. S20), which is equivalent to an ultrahigh cumulative plated capacity of 5.25 Ah cm⁻², almost 65 times greater than that achieves using ZSO electrolyte. Optimal protection is achieved with a Phe additive concentration of 20 mmol L⁻¹, outperforming concentrations of 50 and 100 mmol L⁻¹ (Fig. S21). As indicated in Fig. S22, the Zn||Zn symmetric cells employing 20 mmol L⁻¹ Phe electrolyte exhibit greater charge transfer resistance (R_{ct}) compared with ZSO electrolyte before cycles. This may be attributed to the Phe molecules adsorption layer on Zn anode surface. Significantly, the R_{ct} of battery using ZSO/Phe electrolyte decreases after 10 cycles, which implies the enhanced Zn²⁺ conductivity of organic-inorganic dual-protective SEI. On the contrary, the R_{ct} of batteries using ZSO electrolyte remarkably increases due to rampant Zn dendrites growth and Zn₄(OH)₆(SO₄)₄·5H₂O insulating species formation that blocks Zn²⁺ transport path. In addition, the EIS curves of Zn||Zn symmetric cells cycled in 20 mmol L⁻¹ Phe electrolyte exhibit a smaller R_{ct} than 50 and 100 mmol L⁻¹ Phe that contributes to improve the electrode reaction kinetics for Zn/Zn²⁺ redox (Fig. S23). Moreover, the protection effect of the Phe additive is validated under more harsh

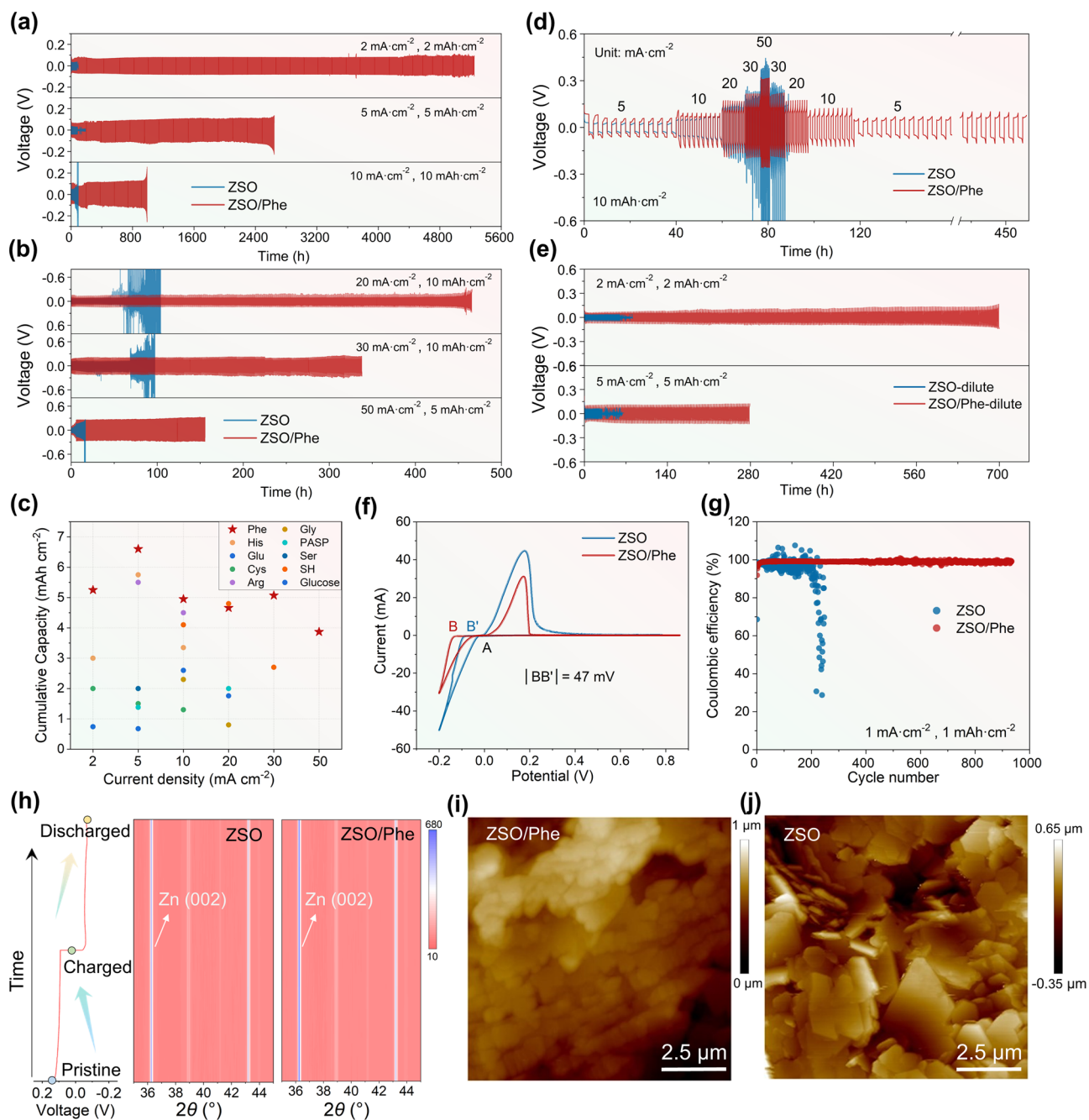


Fig. 4 Reversible Zn plating/stripping stability characterization. **a, b** Long-term galvanostatic cycling of Zn||Zn cells at current density of 2, 5, 10, 20, 30, and 50 mA cm⁻², respectively. **c** Comparison of cumulative plated capacity with previously reported. **d** Rate performances of Zn||Zn cells in different electrolytes. **e** Galvanostatic cycling of Zn||Zn cells in diluted electrolyte. **f** CV curves for Zn nucleation of Zn-Ti cells in different electrolytes. **g** CE of the Zn plating/stripping in Zn||Cu cells. **h** *In situ* XRD measurements on Zn||Zn cells during charging/discharging process. **i, j** AFM images of the cycled Zn in different electrolytes

conditions, showcasing superior cycling stability of 2645 h at 5 mA cm⁻², 990 h at 10 mA cm⁻², 466 h at 20 mA cm⁻², 338 h at 30 mA cm⁻², and 155 h at 50 mA cm⁻², respectively, (Figs. 4a, b and S24). These cumulative plated

capacities surpass most reported Zn metal anode protection strategies, including seven other amino acid additives (Figs. 4c and Table S1) [25, 33, 48, 53–58]. Besides, the rate performances of Zn||Zn symmetrical cells were investigated

simultaneously. While the cell with bare electrolyte experiences severe voltage fluctuation at 20 mA cm^{-2} , the cell with ZSO/Phe electrolyte maintains a stable voltage profile across various current densities of 5, 10, 20, 30, and 50 mA cm^{-2} , sustaining stability for over 460 h even when the current density reverted to 5 mA cm^{-2} (Fig. 4d). This exemplifies the Phe additive's exceptional capability in regulating Zn plating and stripping kinetics. Significantly, even when the electrolyte concentration is diluted tenfold, the Zn anode cycled in ZSO-/Phe-dilute electrolyte also shows stable Zn deposition, surpassing 700 h at 2 mA cm^{-2} , 2 mAh cm^{-2} , and 279 h at 5 mA cm^{-2} , 5 mAh cm^{-2} (Fig. 4e). This reaffirms the practical feasibility of Phe additive utilization in AZIBs. To investigate the nucleation process, cyclic voltammetry (CV) curves were conducted on Zn//Ti half cells. As obtained from Fig. 4f, the cell with ZSO/Phe electrolyte demonstrates an improved nucleation overpotential of 47 mV due to the enhanced reaction energy barrier of Zn deposition caused by the presence of Phe molecules adsorption layer (Fig. S25), which is conducive to drive smaller nucleus radius as well as promote smooth and fine-grained Zn deposits [59]. Consequently, the Zn//Cu half cells maintain excellent Zn plating/stripping reversibility for 934 cycles with an average coulombic efficiency (CE) of 99% (Fig. 4g). The corresponding voltage profiles are displayed in Fig. S26, where moderate voltage hysteresis of 118 mV and stable CE exportation are observed. Contrarily, the cells using ZSO electrolyte experience fluctuating CE, dropping sharply to 30.7% at 218 cycles due to continuous side reactions at deteriorating interfaces. Remarkably, the Zn//Cu half cells cycled in ZSO-/Phe-dilute electrolyte maintain a higher average CE of 98.4% within 218 cycles (Fig. S27). This underscores the overwhelming superiority of the Phe additive in enhancing the reversibility of Zn anode.

Subsequently, *in situ* XRD measurements were taken on Zn//Zn symmetrical cells to explore the Zn deposition behavior optimized by Phe additive. As depicted in Fig. 4h, the Zn anode cycled in ZSO/Phe electrolyte always delivers a stronger characteristic peak of Zn (002) crystal plane at around 36.2° compared to that in ZSO electrolyte during the plating/stripping process, indicating that the Phe molecules adsorption layer guides the preferential Zn nucleation with favorable (002) plane at initial plating stage, thereby inducing Zn^{2+} uniform deposition [47]. This result is consistent with the HRTEM measurement. In addition, the Zn deposition morphology was further investigated by atomic force

microscope (AFM). The Zn anode cycled in ZSO electrolyte exhibits numerous lamellar Zn deposition structure with anisotropic (Fig. 4j), which may enlarge the contact areas between electrode and electrolyte, thus leading to severe corrosion reactions without interrupting [60]. Notably, a dense and smooth Zn deposition layer can be observed in ZSO/Phe electrolyte (Fig. 4i), which is responsible for the superior cycling stability and reaction reversibility of Zn anode even in harsh conditions. On larger scales, the SEM measurements of the deposited Zn metal for 5 cycles at 1, 2, and 5 mA cm^{-2} and 5 mA cm^{-2} were taken (Figs. S28 and S29). The Zn anode cycled in ZSO electrolyte exhibits numerous irregular structures, and the deposition morphology tends to get more looser with higher current densities. On the contrary, the Zn anode cycled in ZSO/Phe electrolyte exhibits a smooth and dendrite-free Zn deposition morphology even at higher current density, which further testify the unique regulation of amphipathic groups in Phe compound for dendrite-free Zn deposition.

3.5 Zn//LMO Full Cell Performance

Ultimately, the electrochemical performances of the full cells comprising LMO cathode and Zn anode were tested to validate the practicability of Phe-contained electrolytes. The CV curves of Zn//LMO full cells using ZSO and ZSO/Phe electrolytes all exhibit a pair of redox peaks (Fig. S30). Figure 5a displays the long-term cycling performance of full cells employing ZSO/Phe electrolyte at current density of 1 C (148 mA g^{-1}), where a considerable initial capacity of 106.9 mAh g^{-1} and a high capacity retention of 77.3% after 300 cycles are achieved, significantly outperforming the ZSO system that retaining only 27.9% of the initial capacity after 125 cycles. Benefiting from the triple protection of Phe additive, including solvation structure regulation, amphipathic molecular adsorption, and organic–inorganic hybrid SEI formation, the Zn//LMO full cell delivers highly consistent charge/discharge profile (Fig. 5b) and smooth Zn anode (Fig. 5d). In sharp contrast, the severe dendrite growth and corrosion sites occurred in the ZSO system (Fig. 5e) may gobble up the Zn anode while exhausting the electrolyte, undoubtedly resulting in the capacity fading and CE decreasing (Fig. 5c). Furthermore, the ZnSO_4 -based electrolyte concentration is diluted by 10 times to testify the modification of Phe additive on reversibility of Zn anode,

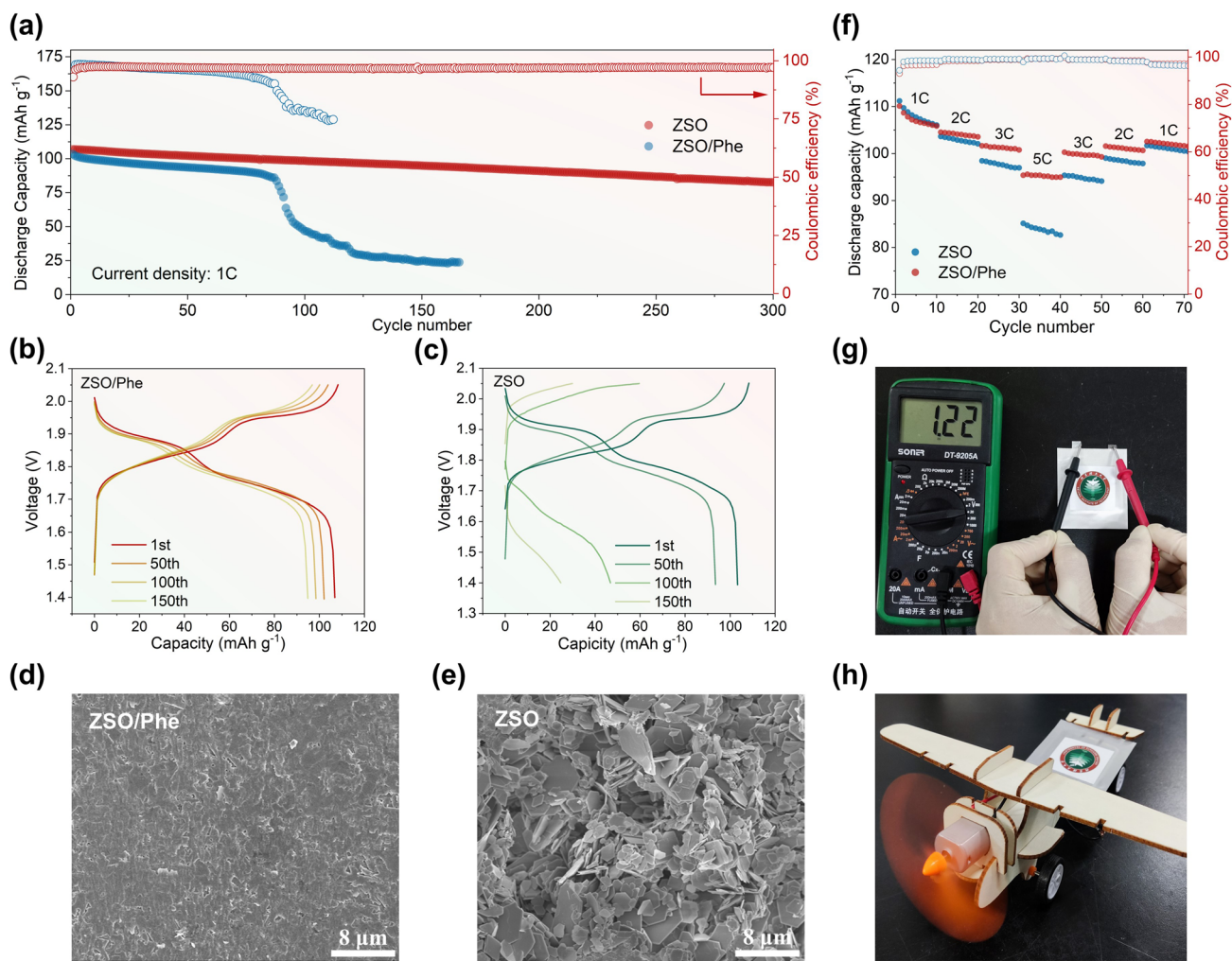


Fig. 5 Zn||LMO full cell performance. **a** Long-term cycling performance at a current density of 1 C. The corresponding voltage–capacity profile in **b** ZSO/Phe and **c** ZSO electrolytes. SEM images of cycled Zn anode in ZSO/Phe **d** ZSO **e** electrolytes. **f** Rate performance at rates of 1, 2, 3, and 5 C. **g, h** Digital photo of open-circuit voltage for the pouch Zn||LMO cell and a model airplane in action powered by Zn||LMO cell

where the Zn||LMO full cells employing ZSO-/Phe-dilute electrolyte exhibits stable capacity output that 55% capacity retention after 100 cycles (Fig. S31), whereas the system of ZSO-dilute electrolyte without additive participation displays a sharp capacity decline and lower CE at initial charging/discharging process. It is more notable that the Zn||LMO full cells with ZSO/Phe electrolyte display superior rate performance, corresponding to a higher average discharge capacity of 95.2 mAh g^{-1} with CE of 99.2% at 5 C and a reversible specific capacity of 102.1 mAh g^{-1} after returning to 1 C (Fig. 5f), which outperforms the ZSO system of exhibiting lower rate capacity of 83.8 mAh g^{-1} at 5 C. Subsequently, a single-layer pouch cell was assembled

with ZSO/Phe electrolyte to successfully drive the airplane model moving toward (Fig. 5g, h), which further verify the practical application of Phe additive in AZIBs.

4 Conclusion

In conclusion, we have introduced the highly biocompatible amino acids molecules as electrolyte additive into AZIBs to address the issues of Zn anode corrosion and regulate the Zn^{2+} uniform deposition. The Phe molecule featuring benzene ring ligands embraces higher adsorption energy for Zn anode to constitute a protective layer for synergistically

homogenizing Zn^{2+} distribution and insulating water molecules, while the adjacent hydroxyl and carboxyl groups incline to form chelating bonds with Zn^{2+} through lone pair electrons, rendering efficient solvation based on Zn^{2+} -Phe coordination for weakening the reactivity of H_2O molecules. Moreover, the preferential reduction of Phe molecules prior to H_2O promotes *in situ* formation of organic–inorganic hybrid SEI for enhancing the interfacial stability of the Zn anode. Benefiting from the triple protection of Phe containing electrolyte, all of the Zn||Zn, Zn||Cu, and Zn||LMO cells display significantly improved electrochemical performances. Even at extreme diluted electrolytes, the Zn anode still exhibits an ultralong cycle life of 700 h under the condition of 2 mA cm^{-2} , 2 mAh cm^{-2} , confirming the feasibility of the electrolyte engineering for practical applications in AZIBs.

Acknowledgements This work was supported by the Joint Funds of the National Natural Science Foundation of China (U2130204), the National Natural Science Foundation of China (52002022), the Young Elite Scientists Sponsorship Program by CAST (YESS20200364), and the Beijing Outstanding Young Scientists Program (BJJWZYJH01201910007023).

Declarations

Conflict of interest The authors declare no interest conflict. They have no known competing financial interests or personal relationships that could have appeared to influence the work reported in this paper.

Open Access This article is licensed under a Creative Commons Attribution 4.0 International License, which permits use, sharing, adaptation, distribution and reproduction in any medium or format, as long as you give appropriate credit to the original author(s) and the source, provide a link to the Creative Commons licence, and indicate if changes were made. The images or other third party material in this article are included in the article's Creative Commons licence, unless indicated otherwise in a credit line to the material. If material is not included in the article's Creative Commons licence and your intended use is not permitted by statutory regulation or exceeds the permitted use, you will need to obtain permission directly from the copyright holder. To view a copy of this licence, visit <http://creativecommons.org/licenses/by/4.0/>.

Supplementary Information The online version contains supplementary material available at <https://doi.org/10.1007/s40820-024-01380-x>.

References

1. S.A. Hashemi, S. Ramakrishna, A.G. Aberle, Recent progress in flexible–wearable solar cells for self-powered electronic devices. *Energy Environ. Sci.* **13**, 685–743 (2020). <https://doi.org/10.1039/c9ee03046h>
2. S. Lei, Z. Liu, C. Liu, J. Li, B. Lu et al., Opportunities for bio-compatible and safe zinc-based batteries. *Energy Environ. Sci.* **15**, 4911–4927 (2022). <https://doi.org/10.1039/D2EE02267B>
3. Y. Yang, W. Gao, Wearable and flexible electronics for continuous molecular monitoring. *Chem. Soc. Rev.* **48**, 1465–1491 (2019). <https://doi.org/10.1039/C7CS00730B>
4. C. Wang, K. Xia, H. Wang, X. Liang, Z. Yin et al., Advanced carbon for flexible and wearable electronics. *Adv. Mater.* **31**, e1801072 (2019). <https://doi.org/10.1002/adma.201801072>
5. X. Xiao, X. Xiao, Y. Zhou, X. Zhao, G. Chen et al., An ultrathin rechargeable solid-state zinc ion fiber battery for electronic textiles. *Sci. Adv.* **7**, eabl3742 (2021). <https://doi.org/10.1126/sciadv.abl3742>
6. X. Jia, C. Liu, Z.G. Neale, J. Yang, G. Cao, Active materials for aqueous zinc ion batteries: synthesis, crystal structure, morphology, and electrochemistry. *Chem. Rev.* **120**, 7795–7866 (2020). <https://doi.org/10.1021/acs.chemrev.9b00628>
7. C. Xu, B. Li, H. Du, F. Kang, Energetic zinc ion chemistry: the rechargeable zinc ion battery. *Angew. Chem. Int. Ed. Engl.* **51**, 933–935 (2012). <https://doi.org/10.1002/anie.201106307>
8. L. Zhang, L. Chen, X. Zhou, Z. Liu, Towards high-voltage aqueous metal-ion batteries beyond 1.5 V: the zinc/zinc hexacyanoferrate system. *Adv. Energy Mater.* **5**, 1400930 (2015). <https://doi.org/10.1002/aenm.201400930>
9. N. Zhang, F. Cheng, J. Liu, L. Wang, X. Long et al., Rechargeable aqueous zinc–manganese dioxide batteries with high energy and power densities. *Nat. Commun.* **8**, 405 (2017). <https://doi.org/10.1038/s41467-017-00467-x>
10. M. Li, C. Wang, Z. Chen, K. Xu, J. Lu, New concepts in electrolytes. *Chem. Rev.* **120**, 6783–6819 (2020). <https://doi.org/10.1021/acs.chemrev.9b00531>
11. S. Wang, G. Liu, L. Wang, Crystal facet engineering of photoelectrodes for photoelectrochemical water splitting. *Chem. Rev.* **119**, 5192–5247 (2019). <https://doi.org/10.1021/acs.chemrev.8b00584>
12. X.-W. Yu, Z. Li, X. Wu, H. Zhang, Q. Zhao et al., Ten concerns of Zn metal anode for rechargeable aqueous zinc batteries. *Joule* **6**, 1145–1175 (2023). <https://doi.org/10.1016/j.joule.2023.05.004>
13. Y.-X. Huang, F. Wu, R.-J. Chen, Thermodynamic analysis and kinetic optimization of high-energy batteries based on multi-electron reactions. *Natl. Sci. Rev.* **7**, 1367–1386 (2020). <https://doi.org/10.1093/nsr/nwaa075>
14. F. Wan, L. Zhang, X. Dai, X. Wang, Z. Niu et al., Aqueous rechargeable zinc/sodium vanadate batteries with enhanced performance from simultaneous insertion of dual carriers.



- Nat. Commun. **9**, 1656 (2018). <https://doi.org/10.1038/s41467-018-04060-8>
15. S.-J. Zhang, J. Hao, D. Luo, P.-F. Zhang, B. Zhang et al., Dual-function electrolyte additive for highly reversible Zn anode. *Adv. Energy Mater.* **11**, 2102010 (2021). <https://doi.org/10.1002/aenm.202102010>
 16. J. Chen, X. Qiao, X. Han, J. Zhang, H. Wu et al., Releasing plating induced stress for highly reversible aqueous Zn metal anodes. *Nano Energy* **103**, 107814 (2022). <https://doi.org/10.1016/j.nanoen.2022.107814>
 17. W. Wang, G. Huang, Y. Wang, Z. Cao, L. Cavallo et al., Organic acid etching strategy for dendrite suppression in aqueous zinc-ion batteries. *Adv. Energy Mater.* **12**, 2102797 (2022). <https://doi.org/10.1002/aenm.202102797>
 18. C. Xie, H. Ji, Q. Zhang, Z. Yang, C. Hu et al., High-index zinc facet exposure induced by preferentially orientated substrate for dendrite-free zinc anode. *Adv. Energy Mater.* **13**, 2203203 (2023). <https://doi.org/10.1002/aenm.202203203>
 19. R. Zhao, X. Dong, P. Liang, H. Li, T. Zhang et al., Prioritizing hetero-metallic interfaces via thermodynamics inertia and kinetics zincophilia metrics for tough Zn-based aqueous batteries. *Adv. Mater.* **35**, e2209288 (2023). <https://doi.org/10.1002/adma.202209288>
 20. S. Chen, J. Chen, X. Liao, Y. Li, W. Wang et al., Enabling low-temperature and high-rate Zn metal batteries by activating Zn nucleation with single-atomic sites. *ACS Energy Lett.* **7**, 4028–4035 (2022). <https://doi.org/10.1021/acscenergylett.2c02042>
 21. J. Han, H. Euchner, M. Kuenzel, S.M. Hosseini, A. Groß et al., A thin and uniform fluoride-based artificial interphase for the zinc metal anode enabling reversible Zn/MnO₂ batteries. *ACS Energy Lett.* **6**, 3063–3071 (2021). <https://doi.org/10.1021/acscenergylett.1c01249>
 22. X. He, Y. Cui, Y. Qian, Y. Wu, H. Ling et al., Anion concentration gradient-assisted construction of a solid-electrolyte interphase for a stable zinc metal anode at high rates. *J. Am. Chem. Soc.* **144**, 11168–11177 (2022). <https://doi.org/10.1021/jacs.2c01815>
 23. L. Cao, D. Li, T. Pollard, T. Deng, B. Zhang et al., Fluorinated interphase enables reversible aqueous zinc battery chemistries. *Nat. Nanotechnol.* **16**, 902–910 (2021). <https://doi.org/10.1038/s41565-021-00905-4>
 24. L. Ma, J. Vatamanu, N.T. Hahn, T.P. Pollard, O. Borodin et al., Highly reversible Zn metal anode enabled by sustainable hydroxyl chemistry. *Proc. Natl. Acad. Sci. U.S.A.* **119**, e2121138119 (2022). <https://doi.org/10.1073/pnas.2121138119>
 25. P. Sun, L. Ma, W. Zhou, M. Qiu, Z. Wang et al., Simultaneous regulation on solvation shell and electrode interface for dendrite-free Zn ion batteries achieved by a low-cost glucose additive. *Angew. Chem. Int. Ed.* **60**, 18247–18255 (2021). <https://doi.org/10.1002/anie.202105756>
 26. W. Yang, X. Du, J. Zhao, Z. Chen, J. Li et al., Hydrated eutectic electrolytes with ligand-oriented solvation shells for long-cycling zinc-organic batteries. *Joule* **4**, 1557–1574 (2020). <https://doi.org/10.1016/j.joule.2020.05.018>
 27. H. Wang, A. Zhou, X. Hu, Z. Hu, F. Zhang et al., Bifunctional dynamic adaptive interphase reconfiguration for zinc deposition modulation and side reaction suppression in aqueous zinc ion batteries. *ACS Nano* **17**, 11946–11956 (2023). <https://doi.org/10.1021/acsnano.3c04155>
 28. A. Zhou, H. Wang, X. Hu, F. Zhang, Y. Zhao et al., Molecular recognition effect enabled by novel crown ether as macrocyclic host towards highly reversible Zn anode. *Sci. Bull.* **68**, 2170–2179 (2023). <https://doi.org/10.1016/j.scib.2023.08.024>
 29. Z. Huang, Z. Li, Y. Wang, J. Cong, X. Wu et al., Regulating Zn(002) deposition toward long cycle life for Zn metal batteries. *ACS Energy Lett.* **8**, 372–380 (2023). <https://doi.org/10.1021/acscenergylett.2c02359>
 30. T.C. Li, Y. Lim, X.L. Li, S. Luo, C. Lin et al., A universal additive strategy to reshape electrolyte solvation structure toward reversible Zn storage. *Adv. Energy Mater.* **12**, 2103231 (2022). <https://doi.org/10.1002/aenm.202103231>
 31. L. Zhou, F. Wang, F. Yang, X. Liu, Y. Yu et al., Unshared pair electrons of zincophilic lewis base enable long-life Zn anodes under “three high” conditions. *Angew. Chem. Int. Ed. Engl.* **61**, e202208051 (2022). <https://doi.org/10.1002/anie.202208051>
 32. X. Shi, J. Wang, F. Yang, X. Liu, Y. Yu et al., Metallic zinc anode working at 50 and 50mAhcm⁻² with high depth of discharge via electrical double layer reconstruction. *Adv. Funct. Mater.* **33**, 2211917 (2023). <https://doi.org/10.1002/adfm.202211917>
 33. H. Lu, X. Zhang, M. Luo, K. Cao, Y. Lu et al., Amino acid-induced interface charge engineering enables highly reversible Zn anode. *Adv. Funct. Mater.* **31**, 2103514 (2021). <https://doi.org/10.1002/adfm.202103514>
 34. Y. Li, P. Wu, W. Zhong, C. Xie, Y. Xie et al., A progressive nucleation mechanism enables stable zinc stripping–plating behavior. *Energy Environ. Sci.* **14**, 5563–5571 (2021). <https://doi.org/10.1039/D1EE01861B>
 35. J. Yang, Y. Zhang, Z. Li, X. Xu, X. Su et al., Three birds with one stone: tetramethylurea as electrolyte additive for highly reversible Zn-metal anode. *Adv. Funct. Mater.* **32**, 2209642 (2022). <https://doi.org/10.1002/adfm.202209642>
 36. Z. Luo, Y. Xia, S. Chen, X. Wu, R. Zeng et al., Synergistic “anchor-capture” enabled by amino and carboxyl for constructing robust interface of Zn anode. *Nano-Micro Lett.* **15**, 205 (2023). <https://doi.org/10.1007/s40820-023-01171-w>
 37. G. Gece, S. Bilgiç, A theoretical study on the inhibition efficiencies of some amino acids as corrosion inhibitors of nickel. *Corros. Sci.* **52**, 3435–3443 (2010). <https://doi.org/10.1016/j.corsci.2010.06.015>
 38. D. Li, Y. Tang, S. Liang, B. Lu, G. Chen et al., Self-assembled multilayers direct a buffer interphase for long-life aqueous zinc-ion batteries. *Energy Environ. Sci.* **16**, 3381–3390 (2023). <https://doi.org/10.1039/D3EE01098H>
 39. B. Niu, Z. Li, D. Luo, X. Ma, Q. Yang et al., Nano-scaled hydrophobic confinement of aqueous electrolyte by a nonionic amphiphilic polymer for long-lasting and wide-temperature

- Zn-based energy storage. *Energy Environ. Sci.* **16**, 1662–1675 (2023). <https://doi.org/10.1039/D2EE04023A>
40. X. Gan, J. Tang, X. Wang, L. Gong, I. Zhitomirsky et al., Aromatic additives with designed functions ameliorating chemomechanical reliability for zinc-ion batteries. *Energy Storage Mater.* **59**, 102769 (2023). <https://doi.org/10.1016/j.ensm.2023.102769>
 41. H.J.C. Berendsen, D. van der Spoel, R. van Drunen, GROMACS: a message-passing parallel molecular dynamics implementation. *Comput. Phys. Commun.* **91**, 43–56 (1995). [https://doi.org/10.1016/0010-4655\(95\)00042-e](https://doi.org/10.1016/0010-4655(95)00042-e)
 42. Y. Duan, C. Wu, S. Chowdhury, M.C. Lee, G. Xiong et al., A point-charge force field for molecular mechanics simulations of proteins based on condensed-phase quantum mechanical calculations. *J. Comput. Chem.* **24**, 1999–2012 (2003). <https://doi.org/10.1002/jcc.10349>
 43. T. Lu, F. Chen, Multiwfn: a multifunctional wavefunction analyzer. *J. Comput. Chem.* **33**, 580–592 (2012). <https://doi.org/10.1002/jcc.22885>
 44. S.J. Clark, M.D. Segall, C.J. Pickard, P.J. Hasnip, M.I.J. Probert et al., First principles methods using CASTEP. *Z. Für Kristallogr. Cryst. Mater.* **220**, 567–570 (2005). <https://doi.org/10.1524/zkri.220.5.567.65075>
 45. J. Wan, R. Wang, Z. Liu, L. Zhang, F. Liang et al., A double-functional additive containing nucleophilic groups for high-performance Zn-ion batteries. *ACS Nano* **17**, 1610–1621 (2023). <https://doi.org/10.1021/acsnano.2c11357>
 46. H. Yang, Z. Chang, Y. Qiao, H. Deng, X. Mu et al., Constructing a super-saturated electrolyte front surface for stable rechargeable aqueous zinc batteries. *Angew. Chem. Int. Ed. Engl.* **59**, 9377–9381 (2020). <https://doi.org/10.1002/anie.202001844>
 47. D. Wang, D. Lv, H. Liu, S. Zhang, C. Wang et al., *In situ* formation of nitrogen-rich solid electrolyte interphase and simultaneous regulating solvation structures for advanced Zn metal batteries. *Angew. Chem. Int. Ed.* **61**, e202212839 (2022). <https://doi.org/10.1002/anie.202212839>
 48. Y. Liu, Y. An, L. Wu, J. Sun, F. Xiong et al., Interfacial chemistry modulation via amphoteric *glycine* for a highly reversible zinc anode. *ACS Nano* **17**, 552–560 (2023). <https://doi.org/10.1021/acsnano.2c09317>
 49. C. Meng, W.-D. He, H. Tan, X.-L. Wu, H. Liu et al., A eutectic electrolyte for an ultralong-lived Zn/V₂O₅ cell: an *in situ* generated gradient solid-electrolyte interphase. *Energy Environ. Sci.* **16**, 3587–3599 (2023). <https://doi.org/10.1039/D3EE01447A>
 50. L. Cao, D. Li, E. Hu, J. Xu, T. Deng et al., Solvation structure design for aqueous Zn metal batteries. *J. Am. Chem. Soc.* **142**, 21404–21409 (2020). <https://doi.org/10.1021/jacs.0c09794>
 51. J. Xu, W. Lv, W. Yang, Y. Jin, Q. Jin et al., *In situ* construction of protective films on Zn metal anodes *via* natural protein additives enabling high-performance zinc ion batteries. *ACS Nano* **16**, 11392–11404 (2022). <https://doi.org/10.1021/acsnano.2c05285>
 52. Y. Zhao, R. Zhou, Z. Song, X. Zhang, T. Zhang et al., Interfacial designing of MnO₂ half-wrapped by aromatic polymers for high-performance aqueous zinc-ion batteries. *Angew. Chem. Int. Ed.* **61**, e202212231 (2022). <https://doi.org/10.1002/anie.202212231>
 53. Y. Wang, L.-E. Mo, X. Zhang, Y. Ren, T. Wei et al., Facet-termination promoted uniform Zn (100) deposition for high-stable zinc-ion batteries. *Adv. Energy Mater.* **13**, 2301517 (2023). <https://doi.org/10.1002/aenm.202301517>
 54. Z. Zhao, P. Li, Z. Zhang, H. Zhang, G. Li, Dendrite-free zinc anode enabled by Buffer-like additive *via* strong cationic specific absorption. *Chem. Eng. J.* **454**, 140435 (2023). <https://doi.org/10.1016/j.cej.2022.140435>
 55. T. Zhou, Y. Mu, L. Chen, D. Li, W. Liu et al., Toward stable zinc aqueous rechargeable batteries by anode morphology modulation *via* polyaspartic acid additive. *Energy Storage Mater.* **45**, 777–785 (2022). <https://doi.org/10.1016/j.ensm.2021.12.028>
 56. Y. Liu, J. Wang, J. Sun, F. Xiong, Q. Liu et al., A glutamate anion boosted zinc anode for deep cycling aqueous zinc ion batteries. *J. Mater. Chem. A* **10**, 25029–25038 (2022). <https://doi.org/10.1039/D2TA06975J>
 57. Q. Wen, H. Fu, Z.-Y. Wang, Y.-D. Huang, Z.-J. He et al., A hydrophobic layer of amino acid enabling dendrite-free Zn anodes for aqueous zinc-ion batteries. *J. Mater. Chem. A* **10**, 17501–17510 (2022). <https://doi.org/10.1039/D2TA04015H>
 58. Y. Li, Y. Wang, Y. Xu, W. Tian, J. Wang et al., Dynamic biomolecular “mask” stabilizes Zn anode. *Small* **18**, 2202214 (2022). <https://doi.org/10.1002/sml.202202214>
 59. Z. Hu, F. Zhang, A. Zhou, X. Hu, Q. Yan et al., Highly reversible Zn metal anodes enabled by increased nucleation overpotential. *Nano-Micro Lett.* **15**, 171 (2023). <https://doi.org/10.1007/s40820-023-01136-z>
 60. H. Wang, A. Zhou, Z. Hu, X. Hu, F. Zhang et al., Toward simultaneous dense zinc deposition and broken side-reaction loops in the Zn/V₂O₅ system. *Angew. Chem. Int. Ed.* (2024). <https://doi.org/10.1002/anie.202318928>

